nature materials

ARTICLES

PUBLISHED ONLINE: 15 AUGUST 2016 | DOI: 10.1038/NMAT4724

Anisotropic phase segregation and migration of Pt in nanocrystals en route to nanoframe catalysts

Zhiqiang Niu[1†], Nigel Becknell[1†], Yi Yu[1,2], Dohyung Kim[3], Chen Chen[1,4], Nikolay Kornienko[1], Gabor A. Somorjai[1,2,5] and Peidong Yang[1,2,3,5★]

Compositional heterogeneity in shaped, bimetallic nanocrystals offers additional variables to manoeuvre the functionality of the nanocrystal. However, understanding how to manipulate anisotropic elemental distributions in a nanocrystal is a great challenge in reaching higher tiers of nanocatalyst design. Here, we present the evolutionary trajectory of phase segregation in Pt–Ni rhombic dodecahedra. The anisotropic growth of a Pt-rich phase along the ⟨111⟩ and ⟨200⟩ directions at the initial growth stage results in Pt segregation to the 14 axes of a rhombic dodecahedron, forming a highly branched, Pt-rich tetradecapod structure embedded in a Ni-rich shell. With longer growth time, the Pt-rich phase selectively migrates outwards through the 14 axes to the 24 edges such that the rhombic dodecahedron becomes a Pt-rich frame enclosing a Ni-rich interior phase. The revealed anisotropic phase segregation and migration mechanism offers a radically different approach to fabrication of nanocatalysts with desired compositional distributions and performance.

Metal nanocatalysts are an important sector of heterogeneous catalysis because their high surface-to-mass ratio allows for efficient use of expensive, catalytically active transition metals[1]. Discovery of novel nanocatalysts is vital in increasing catalytic efficiency to conserve energy and precious metals in various processes[2]. Two strategies heavily utilized in the discovery of novel nanocatalysts are composition[3] and shape[4,5] control. These approaches, in particular, have been central to the advancement of oxygen reduction electrocatalysis. Platinum alloys have shown dramatic improvement over pure platinum[6–8], and platinum–nickel octahedra have consistently demonstrated activity improvements over their spherical counterparts[9–14]. However, new strategies are needed to push the activity and stability of platinum-based nanocatalysts to more impressive numbers which can make an impact in the fuel cell market[2,15].

One strategy coming to the forefront of catalyst innovation is nanoscopic design of bimetallic catalyst structures through spatial segregation of the elements. Element-specific segregation in the Pt–Ni alloy system has been an intensively studied topic due to the early observation of a Pt-enriched {111} surface after vacuum annealing and its use as an extraordinary model oxygen reduction electrocatalyst[6,16]. Naturally, Pt–Ni octahedral nanocatalysts were synthesized to attempt to replicate the unique nanosegregation of Pt to the {111} facets, but it was observed that {111} facets were Ni-rich, and therefore corroded from the octahedra during electrochemical testing[12]. Recently, an in-depth study by Gan *et al.* explained that, during Pt–Ni octahedra synthesis, platinum was reduced first into hexapod-like concave nanocrystals on which nickel would undergo step-induced growth into the concave surfaces of the hexapod, forming the Ni-rich facets[17]. Oh *et al.* observed similar hexapod-like Pt-rich arms in their Pt–Ni octahedral system, but in the presence of carbon monoxide some Pt then migrated to the edges of the octahedron, creating a structure similar to a nanoframe[18].

Our group observed similar phenomena during the synthesis of $PtNi_3$ and $PtCo_3$ rhombic dodecahedra, which had a Pt-rich phase segregated to their edges[19–21]. Until now, it was not understood how the Pt-rich phase segregated to the edges of the rhombic dodecahedron and what was the driving force for this phenomenon. However, in this work, we have fully described the formation mechanism of Pt–Ni rhombic dodecahedra by analysing the reaction at a slower rate with quasi-*in situ* sampling. The growth is divided into distinct stages of Pt-rich phase segregation and subsequent phase migration. It is found that initially, a Pt-rich seed particle forms on which overgrowth occurs in both the ⟨111⟩ and ⟨200⟩ growth directions. This distinctive bidirectional growth and segregation of the Pt-rich phase structurally guides the formation of the dodecahedron and provides a pathway for Pt atoms to migrate outwards to the vertices and edges of the dodecahedron and become enriched on the edges. By stopping the nanoparticle growth at specific times, the segregation of Pt to the edges of the rhombic dodecahedron can be controlled, and is shown to dictate the oxygen reduction activity of the nanoframes which result from the corrosion of the rhombic dodecahedra.

The Pt–Ni rhombic dodecahedra (RD) were synthesized by hot-injection of metal precursors in oleylamine at a lower synthetic temperature than previously reported (265 °C)[20] to track the growth process over a longer period of time (see Methods). Intermediate structures were captured from the growth solution, which turned from green to yellow, brown, and finally black in about one hour. The initial Pt–Ni nanoparticles (Fig. 1a) collected from the green growth solution had an average size of 3.3 ± 1.4 nm and a composition of $Pt_{70}Ni_{30}$, as determined by energy dispersive X-ray spectroscopy (EDS). Their morphology is either near-spherical (dominated by {111} and {100} facets) or elongated in the ⟨111⟩ or ⟨200⟩ directions as shown in the high-resolution transmission electron microscopy (HRTEM) images (Fig. 1d). When the solution turned yellow, these small nanoparticles had grown into branched structures with a size range of 4–15 nm (Fig. 1b). The growth directions of the short arms

---

[1]Department of Chemistry, University of California, Berkeley, California 94720, USA. [2]Materials Sciences Division, Lawrence Berkeley National Laboratory, Berkeley, California 94720, USA. [3]Department of Materials Science and Engineering, University of California, Berkeley, California 94720, USA. [4]Department of Chemistry, Tsinghua University, Beijing 100084, China. [5]Kavli Energy NanoSciences Institute, Berkeley, California 94720, USA.
[†]These authors contributed equally to this work. *e-mail: p_yang@berkeley.edu

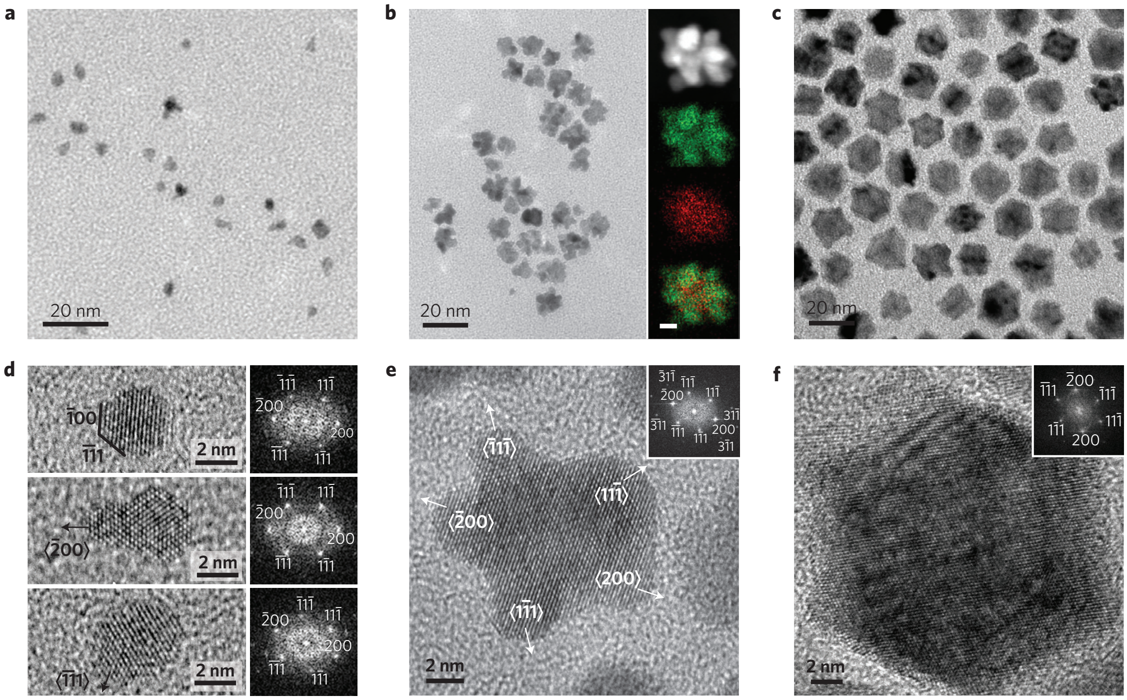

Figure 1 | Formation process of the rhombic dodecahedra. TEM (**a**–**c**) and corresponding HRTEM (**d**–**f**) images of interim products obtained from the growth solution when its colour is green, yellow, and brown, respectively. HAADF-STEM and EDS elemental mapping images (**b**, right) of a typical particle in **b**: green is Pt and red is Ni, scale bar, 2 nm. FFTs of the corresponding HRTEM images (**d**,right; insets in **e** and **f**) indicate the growth directions of elongated nanoparticles and branched nanostructures. Moiré patterns (**f**) indicate the superimposition of two phases with different lattice constants present in the particle[24].

are ⟨111⟩ and ⟨200⟩ (Fig. 1e and Supplementary Fig. 1), identical to those of the initial non-spherical particles. This indicates that the initial small particles serve as seeds on which bidirectional overgrowth occurs along the ⟨111⟩ and ⟨200⟩ directions much faster than other directions[22]. The high-angle annular dark-field scanning transmission electron microscopy (HAADF-STEM) and EDS mapping images of a typical branched particle demonstrate that Pt is homogeneously distributed within the whole particle, whereas Ni is mainly distributed around the centre (Fig. 1b, right). The composition of these branched structures was $Pt_{49}Ni_{51}$. The higher Ni content compared to the initial nanoparticles suggests the reduction of Ni is accelerated during this period, possibly induced by step sites between the arms of the growing branched structures, as indicated in Supplementary Fig. 1c[17,23]. These step sites are located precisely where we observe growth of the Ni-rich phase in EDS mapping. When the growth solution became brown, most branched particles had grown into well-defined polyhedra with an average size of 13 ± 5 nm (Fig. 1c,f). The polyhedra have been identified as rhombic dodecahedra on the basis of typical projections along different zone axes[19]. The Ni content increased significantly to $Pt_{12}Ni_{88}$, which could result from continuous Ni-rich phase deposition on step sites until reaching the top of the arms and filling out the rhombic dodecahedron.

Figure 2a–c shows TEM images of products obtained at 3, 10 and 30 min after the growth solution had turned black. They are denoted as RD-3, RD-10 and RD-30, respectively. The average size is similar for RD-3 (16 nm, standard deviation $\sigma = 1.6$) and RD-10 (17 nm, $\sigma = 2.1$), but increases for RD-30 (22 nm, $\sigma = 2.6$) (Supplementary Fig. 2a). To expose the distribution of the Pt-rich phase in the particles, we selectively removed the Ni-rich phase by chemical corrosion and termed these structures RD-3-cor, RD-10-cor and RD-30-cor, respectively. RD-3 evolved to structures (Fig. 2d and Supplementary Fig. 3) that have multiple long arms with a thickness of 2.1 nm ($\sigma = 0.3$, Supplementary Fig. 2b). The arms are identified as the 14 axes of the parent rhombic dodecahedron stretching from origin to vertex (Supplementary Fig. 4), on the basis of the representative projected geometries (Supplementary Fig. 5a–c). Therefore, RD-3-cor is named a tetradecapod. There are two types of axes in a rhombic dodecahedron, with the crystallography of a face-centred cubic (fcc) alloy dictating that an axis is along either the ⟨111⟩ or ⟨200⟩ directions. The HRTEM and corresponding fast Fourier transforms (FFT, Supplementary Fig. 5d–f) agree perfectly with this model. It should be restated that the ⟨111⟩ and ⟨200⟩ directions are precisely the growth directions of the branched intermediates (Fig. 1e and Supplementary Fig. 1), so the Pt-rich phase had only further segregated to the axes inside RD-3, leaving uniform arms in the RD-3-cor tetradecapod. Alternatively, RD-10 and RD-30 transformed into nanoframes after the corrosion (Fig. 2e,f), consistent with our previous finding[19]. The average thickness of the frames' edges increased from 1.6 nm ($\sigma = 0.2$) for RD-10 to 3.4 nm ($\sigma = 0.6$) for RD-30 (Supplementary Fig. 2b), suggesting more Pt enriched on the edges with prolonged growth time.

The spatial distributions of Pt and Ni in the rhombic dodecahedra at different growth times were further characterized by HAADF-STEM and EDS mapping (Fig. 3a–c). The samples were viewed along the [111] zone axis to compare their hexagonal projections. It clearly shows that Ni is distributed homogeneously in all three stages of the dodecahedron, whereas Pt is mainly distributed on the diagonals of the hexagon for RD-3, and also on the six sides of the hexagon in RD-10 and RD-30. This is consistent with the three-dimensional models in which the Pt-rich phase segregated on the 14 axes for RD-3 and on the 24 edges for RD-10 and RD-30. Notably, RD-30 has much thicker Pt-rich diagonals and sides than RD-10, which were conserved in the corroded product. In RD-3-cor, RD-10-cor and RD-30-cor, the Pt and Ni are distributed homogeneously within the respective tetradecapod or frame, and each has an identical composition of $Pt_{75}Ni_{25}$, based on EDS (Fig. 3d–f).

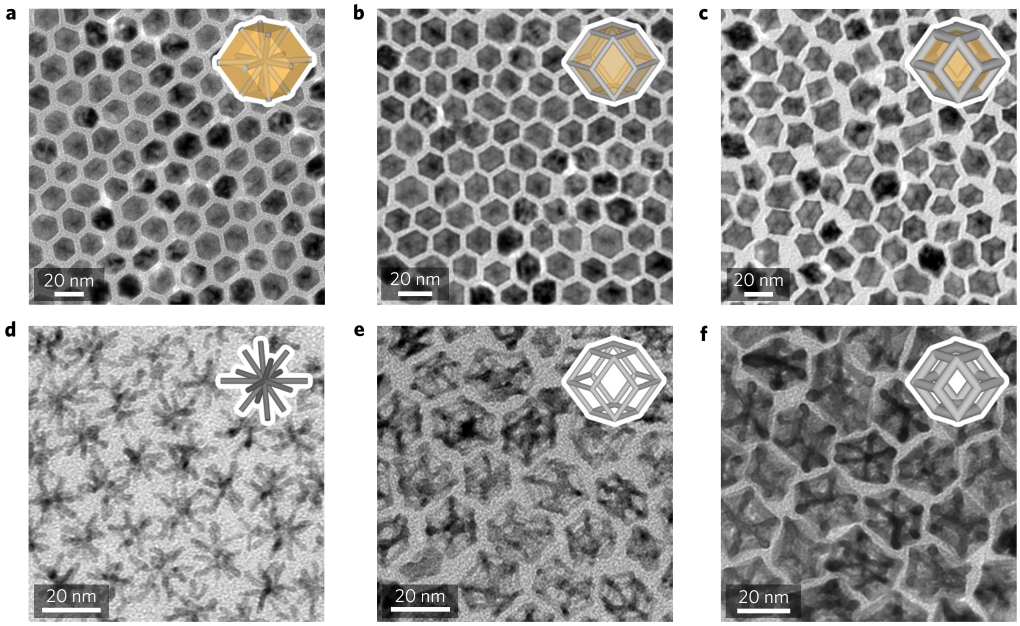

Figure 2 | Development of rhombic dodecahedra and corrosion to three-dimensional nanostructures. a–c, TEM images of rhombic dodecahedra with growth times of 3 min (**a**), 10 min (**b**) and 30 min (**c**) after the growth solution turns black. **d–f**, TEM images of the corresponding products of **a–c** after removal of the Ni-rich phase by selective chemical corrosion, which reveal the morphology of the Pt-rich phase in the parent solid particles. Insets in **a–f** are geometrical models, in which the grey colour represents Pt-rich phase and orange represents Ni-rich phase.

Table 1 | Compositions of RD-3, RD-10 and RD-30 determined by EDS, ICP and XPS.

Method	Ni:Pt atomic ratio		
	RD-3	RD-10	RD-30
EDS	9:1	9:1	3:1
ICP	9:1	9:1	3:1
XPS	15:1	6:1	2:1

The bulk compositions of RD-3, RD-10 and RD-30 determined by EDS coincided well with the inductively coupled plasma optical emission spectroscopy (ICP-OES) results (Table 1). RD-3 and RD-10 possessed the same Ni:Pt ratio (9:1). However, the Ni:Pt ratio drastically decreased to 3:1 for RD-30 due to the continued Pt enrichment on the edges of the dodecahedra. X-ray photoelectron spectroscopy (XPS, Supplementary Fig. 6) showed that Ni enriched on the surface in RD-3, whereas Pt enriched on the surface in RD-10 and RD-30 (Table 1). This is consistent with the structural models.

X-ray diffraction (XRD) patterns of RD-3, RD-10 and RD-30 (Fig. 4a) were used to characterize their distinctive phase segregation. The diffraction peaks of RD-3 and RD-10 are characteristic of the expected fcc alloy. Using Vegard's rule, their compositions are roughly estimated to be Pt_8Ni_{92}, but this does not account for the asymmetry observed in the diffraction peaks. The asymmetry toward the left confirms that there is a segregated Pt-rich phase diffracting at lower 2θ values which coexists with the sharply diffracting Ni-rich phase. With increasing reaction time (RD-30), the asymmetric peaks split into two sets of diffraction patterns, which are assigned to a Pt-rich phase ($Pt_{61}Ni_{39}$) and a Ni-rich phase (Pt_8Ni_{92}), again based on Vegard's rule. The progression of the diffraction patterns from asymmetric peaks to split peaks is clearly shown by stopping the reaction at finer time resolution (Supplementary Fig. 7). The peak position of the Ni-rich phase does not change during the entire growth. It is evident that there is a core Pt_8Ni_{92} phase that does not change composition, while Pt enriches on the edges of the dodecahedra and causes the Pt-rich phase to grow larger in lattice constant and in crystallite size. The XRD patterns of the chemically corroded products are also exhibited in Fig. 4a. The asymmetric and split diffraction peaks become a single set of symmetric peaks after chemical corrosion, indicating one phase with an estimated composition of $Pt_{75}Ni_{25}$ from Vegard's rule.

Phase segregation in the rhombic dodecahedra was further confirmed by extended X-ray absorption fine structure (EXAFS) data taken at the Ni K-edge and Pt L_3-edge (Fig. 4b). For RD-3 and RD-10, the Ni K-edge and Pt L_3-edge EXAFS data were successfully co-fit using paths from a disordered fcc $Pt_{10}Ni_{90}$ model (Supplementary Fig. 8)[26,27]. The EXAFS fit to RD-30 was performed using paths from a $Pt_{25}Ni_{75}$ disordered fcc model. Additional information on the fitting procedure is provided in the Supplementary Information. For each sample, the EXAFS-determined coordination numbers were used to calculate the extent of alloying parameters (Supplementary Table 1)[28], which illustrate that Pt and Ni in RD-30 were significantly more segregated from each other than in either RD-3 or RD-10. This more significant phase segregation led to the peak-splitting observed in the XRD pattern for RD-30, whereas the phase segregation in RD-3 and RD-10 caused only peak asymmetry in the XRD patterns.

An important, yet unaddressed question is how RD-3 with Pt-rich phase segregated to the inner axes progresses to RD-10 with Pt-rich phase segregated to the outer edges. Considering the extremely high similarity of RD-3 and RD-10 in terms of XRD patterns, EXAFS structures, and ICP compositions, we propose that their dissimilar elemental distributions are caused by the outward, anisotropic migration of Pt. One would then anticipate that an intermediate structure between RD-3 and RD-10 would have Pt-rich phase segregation on both axes and edges. As shown in Supplementary Fig. 9, the rhombic dodecahedra turned into incomplete nanoframes with Pt-rich phase remaining on both edges and axes after chemical corrosion. In addition, we attempted the conversion of RD-3 into RD-10 under *ex situ* conditions. If RD-3 was separated from the growth solution and annealed in neat oleylamine at 230 °C under N_2, it could be corroded into nanoframes, rather than tetradecapods, because Pt had migrated from the axes to the edges (Supplementary Fig. 10). These control experiments further

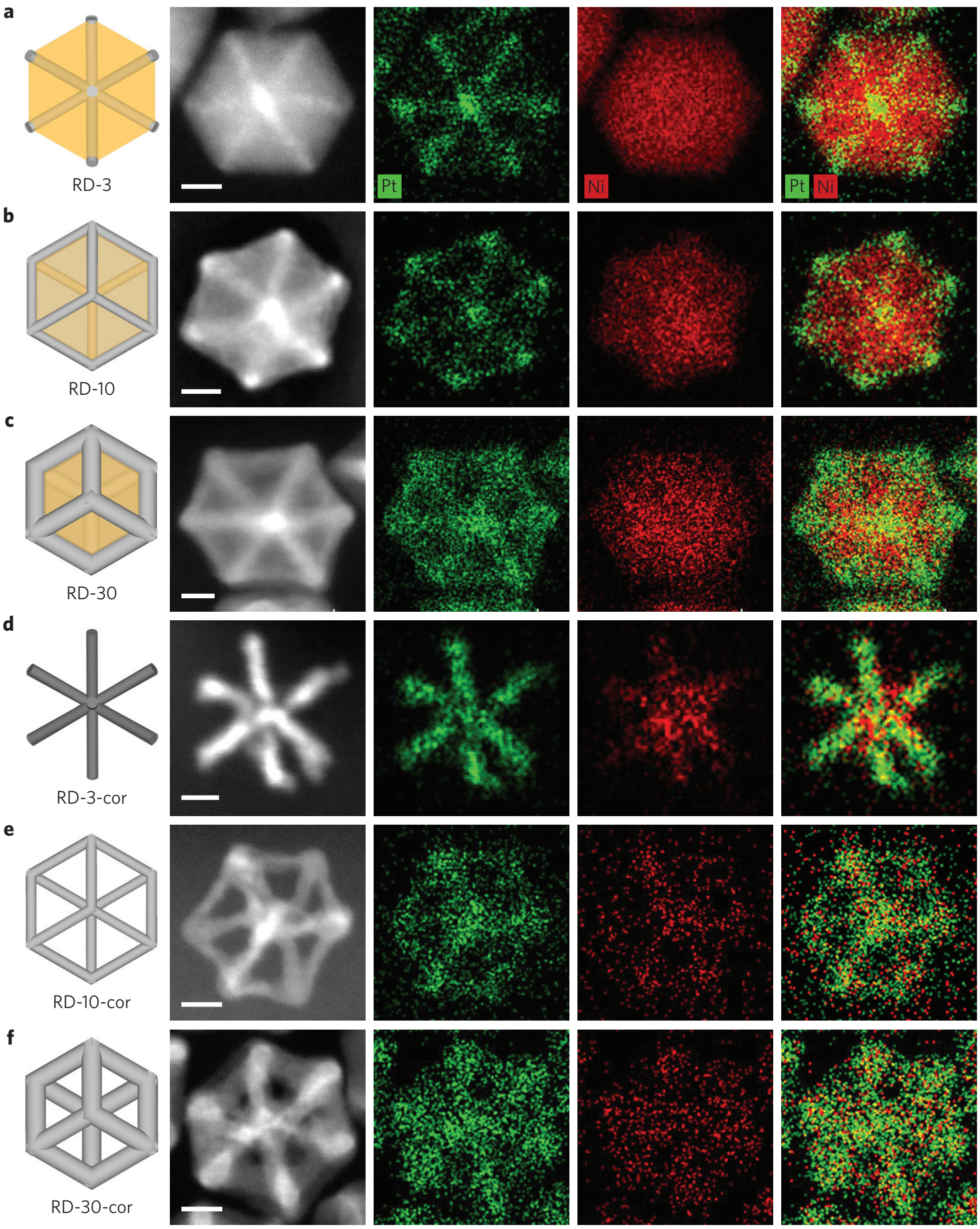

Figure 3 | STEM–EDS analysis of segregation and migration of Pt in Pt–Ni rhombic dodecahedra. a–f, HAADF-STEM and EDS mapping images of rhombic dodecahedra with different growth times of 3 min (**a**), 10 min (**b**) and 30 min (**c**), and their corresponding chemically corroded products (**d–f**). The intensity of the HAADF image is approximately proportional to atomic number $(Z^2)^{25}$. In RD-3, the bright signal represents the Pt-rich arms stretching from the origin to the vertices of the dodecahedron. In RD-10 and RD-30, the bright signal represents the Pt-rich edges of the dodecahedron which construct the nanoframe. In the EDS maps, green colour represents Pt and red colour represents Ni. Whereas Ni is homogeneously distributed in all three types of rhombic dodecahedra, Pt enriches at diagonals for RD-3 and at both diagonals and six sides for RD-10 and RD-30. In all images, scale bar, 6 nm.

illustrate the outward, anisotropic migration of Pt from the axes, although the underlying driving force must still be explained.

In a bimetallic alloy, the overall Gibbs energy of the particle must be minimized during any phase segregation that occurs[29–31]. Preferential elemental segregation to the surface can result from differences in surface energy and/or atomic radius between the two metals. However, the segregation phenomena must overwhelm the influence of the chemical ordering energy of the alloy system[31]. The Pt–Ni system has ordered phases for $Pt_{25}Ni_{75}$ or $Pt_{50}Ni_{50}$ compositions[32,33], but the ordering of a given phase at any stage of the growth is not observed by XRD and is unexpected due to the synthetic temperature used[34]. Therefore, the element with lower surface energy is more likely to segregate to the surface unless a significant strain energy is induced by the larger element (which may or may not have lower surface energy), causing it to surface segregate to reduce the strain. We observe both phenomena in the Pt–Ni rhombic dodecahedron. The rhombic dodecahedral shape exposes exclusively {110} facets, and the surface energies of Pt{110} and Ni{110} are 2.819 and 2.368 J m^{-2}, respectively[35]. Therefore, it is expected that Ni would preferentially segregate to the faces of the dodecahedron. However, Pt is much larger than Ni, with their atomic radii being 1.39 Å (Pt) and 1.24 Å (Ni)[36]. Consequently, the larger Pt atoms on the interior of RD-3 tend to migrate outwards to relieve the internal strain, transitioning to the RD-10 structure. The Pt atoms migrate to vertex and edge sites in RD-10 and RD-30 because Ni-rich facets are highly favoured by the lower surface energy of Ni{110}. The progression from an ill-defined branched structure (Fig. 1b) to a uniform Pt-rich tetradecapod (Fig. 2d and

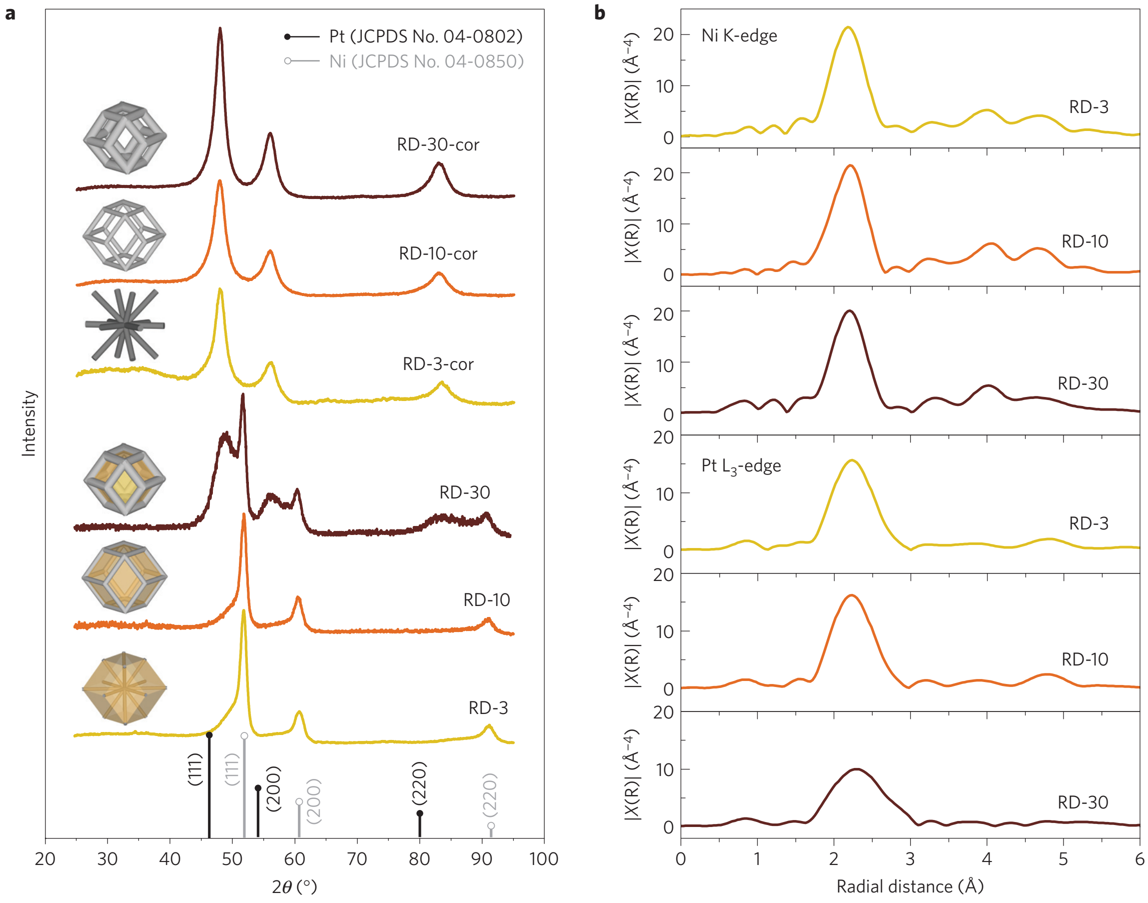

Figure 4 | Structural evolution over time in Pt–Ni rhombic dodecahedra. a, Powder X-ray diffraction patterns of rhombic dodecahedra and their corresponding chemically corroded products. RD-3 and RD-10 show asymmetric diffraction peaks at lower 2Θ that indicate the coexistence of segregated Pt-rich phase. The asymmetric peaks split into two sets of diffraction patterns for RD-30, in which more Pt had grown on the edges. **b**, Ni K-edge and Pt L_3-edge EXAFS spectra of rhombic dodecahedra. RD-3 and RD-10 have similar EXAFS spectra due to their nearly identical bulk compositions, while RD-30 has lower intensity in its first-shell peaks at the Ni K-edge and Pt L_3-edge due to its increased phase segregation and Pt enrichment.

Supplementary Fig. 3) illustrates that Pt furthered its segregation to the axes of the dodecahedron before migrating to the edges. This observation, along with the intermediate structures with partial branch and frame morphology (Supplementary Fig. 9c), implies that RD-3 progresses to RD-10 through migration of Pt along the Pt-rich axes of the dodecahedron to the vertices, and then to the edges. The anisotropic migration is likely guided by the energetic favourability of large Pt atoms diffusing through a Pt-rich phase along the axes, as opposed to diffusing through the Pt_8Ni_{92} phase surrounding the axes in the interior of RD-3 and RD-10[18].

Having thoroughly characterized the typical products obtained in the growth of Pt–Ni rhombic dodecahedra, we can now piece discrete stages together into a whole picture. Figure 5 plots the trend in Pt and Ni content in the products obtained during the whole growth process. From the initial $Pt_{70}Ni_{30}$ nanoparticles, the Ni content increased first to $Pt_{49}Ni_{51}$ for the branched intermediates, and then to $Pt_{12}Ni_{88}$ for the primary rhombic dodecahedra. The substantial increase in Ni content during this period can be attributed to Ni deposition on the low-coordination sites of intermediate structures[17,23], which arose from anisotropic overgrowth of Pt on the non-spherical seeds. The nickel content then increased slightly more, becoming the $Pt_{10}Ni_{90}$ rhombic dodecahedra (RD-3). The Ni:Pt ratio remained nearly unchanged through RD-10. At the same time, Pt segregated to the axes (RD-3) and then migrated through the axes onto the edges (RD-10) to minimize the energy penalties arising from the strain of the larger Pt atoms inside the Ni-rich lattice. After the anisotropic migration, the Pt content slowly increased to $Pt_{35}Ni_{65}$ with increasing growth time (40 min). As the well-defined rhombic dodecahedron has fewer step sites, the Ni deposition becomes greatly suppressed during the Pt enrichment stage. The increase in Pt content comes from continued Pt reduction from the remaining precursor in solution onto the edges of RD-10. The Pt-rich phase migration (RD-3 to RD-10) and enrichment (RD-10 to RD-30) are both selectively onto the edges and not the facets of the rhombic dodecahedra, due to the higher surface energy of Pt{110} than Ni{110}. The comprehensive growth trajectory is presented in Fig. 5.

The results of this study lend insight into novel methods for constructing nanocatalysts with desired performance using designed phase segregation patterns. We have demonstrated this concept by measuring the oxygen reduction activity of RD-3-cor, RD-10-cor and RD-30-cor (Supplementary Fig. 11). The advantage of controlling Pt segregation to the edges of the rhombic dodecahedron is clear in that both the specific activity and mass activity of the open nanostructures can be tuned to higher values by allowing Pt edge segregation to increase. The activity trend observed demonstrates the beneficial effects of tuning morphology and size, which can affect the coordination and strain of surface atoms performing catalysis[12,37].

This work has revealed through Pt–Ni rhombic dodecahedra that the growth of shaped, bimetallic nanostructures is a complex, concurrent evolution of their composition, element spatial distribution, and morphology. Such intricate phenomena are consequences of a series of fundamental chemistries, including

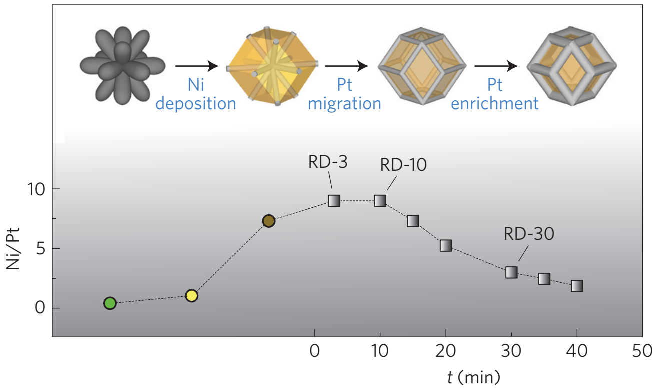

Figure 5 | Summary of the complete growth process of a Pt–Ni rhombic dodecahedron. The composition plot indicates that Ni content in the products increases first and then decreases. Compositions in the plot are determined by EDS for circles and by ICP for squares. The colours of the circular points represent the colours of the growth solution from which the products were obtained. The schematic illustration of the growth mechanism exhibits three growth regimes: Ni deposition on the step sites of Pt-rich branch structures; anisotropic migration of Pt from axes to edges; continued enrichment of Pt on edges. In the scheme, grey colour represents the Pt-rich phase while orange represents the Ni-rich phase.

un-matched reduction potentials of metal precursors, anisotropic overgrowth on preformed seeds, step-induced metal deposition, and site-dependent phase segregation and migration. The growth trajectory of a bimetallic nanostructure therefore relies on how we manoeuvre these fundamental steps. The anisotropic overgrowth can be modified by the type of seed present in the growth solution and the ligand coordination strength to the facets of the seed[38–40]. It is possible that the growth direction could be exclusively along the ⟨111⟩ or ⟨200⟩ directions if the seeds take an octahedral or cubic shape or if ligand binding is favoured on either the {111} or {100} facets. In the growth of Pt–Ni rhombic dodecahedra, the near-spherical seeds had {111} and {100} facets and the overgrowth was bidirectional. Unidirectional overgrowth along the ⟨200⟩ direction was observed in the growth of Pt–Ni octahedra using dimethylformamide DMF-solvated acetylacetonate as the ligand. The final product exhibited a phase segregation pattern with Ni enriched on the {111} facets of the octahedron[17].

After the initial anisotropic growth, anisotropic migration of the segregated phase can further tune the functionality of the nanocrystal. In Pt–Ni rhombic dodecahedra, phase segregation and migration allowed for $Pt_{75}Ni_{25}$ tetradecapods or nanoframes to be obtained after chemical corrosion of nickel inside the particles. The nanoframe structure was previously demonstrated as capable of drastically improving material utility and ORR activity due to its open structure with three-dimensional molecular accessibility. This unique electrocatalyst design was made possible through distinct stages of the nanocrystal growth. Pt-rich anisotropic growth provided the structure-directing seed to form rhombic dodecahedra. The Pt-rich phase then migrated anisotropically through the axes of the dodecahedron to its vertices and edges, which were further enriched with Pt. Our findings highlight the importance of anisotropic growth and site-dependent phase segregation and migration mechanisms for controlling the compositional heterogeneity in bimetallic nanostructures, offering a radically different approach to the fabrication of nanocatalysts with enhanced performance.

Methods

Methods and any associated references are available in the online version of the paper.

Received 22 February 2016; accepted 4 July 2016;

References

1. Bell, A. T. The impact of nanoscience on heterogeneous catalysis. *Science* **299,** 1688–1691 (2003).
2. Debe, M. K. Electrocatalyst approaches and challenges for automotive fuel cells. *Nature* **486,** 43–51 (2012).
3. Ferrando, R., Jellinek, J. & Johnston, R. L. Nanoalloys: from theory to applications of alloy clusters and nanoparticles. *Chem. Rev.* **108,** 845–910 (2008).
4. Narayanan, R. & El-Sayed, M. A. Shape-dependent catalytic activity of platinum nanoparticles in colloidal solution. *Nano Lett.* **4,** 1343–1348 (2004).
5. Xia, Y., Xiong, Y., Lim, B. & Skrabalak, S. E. Shape-controlled synthesis of metal nanocrystals: simple chemistry meets complex physics? *Angew. Chem. Int. Ed.* **48,** 60–103 (2009).
6. Stamenkovic, V. R. *et al*. Improved oxygen reduction activity on Pt_3Ni (111) via increased surface site availability. *Science* **315,** 493–497 (2007).
7. Stamenkovic, V. R. *et al*. Trends in electrocatalysis on extended and nanoscale Pt-bimetallic alloy surfaces. *Nature Mater.* **6,** 241–247 (2007).
8. Wang, C. *et al*. Design and synthesis of bimetallic electrocatalyst with multilayered Pt-skin surfaces. *J. Am. Chem. Soc.* **133,** 14396–14403 (2011).
9. Zhang, J., Yang, H., Fang, J. & Zou, S. Synthesis and oxygen reduction activity of shape-controlled Pt_3Ni nanopolyhedra. *Nano Lett.* **10,** 638–644 (2010).
10. Wu, J. *et al*. Truncated octahedral Pt_3Ni oxygen reduction reaction electrocatalysts. *J. Am. Chem. Soc.* **132,** 4984–4985 (2010).
11. Cui, C. H. *et al*. Octahedral PtNi nanoparticle catalysts: exceptional oxygen reduction activity by tuning the alloy particle surface composition. *Nano Lett.* **12,** 5885–5889 (2012).
12. Cui, C. H., Gan, L., Heggen, M., Rudi, S. & Strasser, P. Compositional segregation in shaped Pt alloy nanoparticles and their structural behaviour during electrocatalysis. *Nature Mater.* **12,** 765–771 (2013).
13. Choi, S.-I. *et al*. Synthesis and characterization of 9 nm Pt–Ni octahedra with a record high activity of 3.3 A/mgPt for the oxygen reduction reaction. *Nano Lett.* **13,** 3420–3425 (2013).
14. Huang, X. *et al*. High-performance transition metal–doped Pt_3Ni octahedra for oxygen reduction reaction. *Science* **348,** 1230–1234 (2015).
15. Gasteiger, H. A. & Markovic, N. M. Just a dream–or future reality? *Science* **324,** 48–49 (2009).
16. Gauthier, Y., Joly, Y., Baudoing, R. & Rundgren, J. Surface-sandwich segregation on nondilute bimetallic alloys: $Pt_{50}Ni_{50}$ and $Pt_{78}Ni_{22}$ probed by low-energy electron diffraction. *Phys. Rev. B* **31,** 6216–6218 (1985).
17. Gan, L. Element-specific anisotropic growth of shaped platinum alloy nanocrystals. *Science* **346,** 1502–1506 (2014).
18. Oh, A. *et al*. Skeletal octahedral nanoframe with cartesian coordinates via geometrically precise nanoscale phase segregation in a Pt@Ni core–shell nanocrystal. *ACS Nano* **9,** 2856–2867 (2015).
19. Chen, C. *et al*. Highly crystalline multimetallic nanoframes with three-dimensional electrocatalytic surfaces. *Science* **343,** 1339–1343 (2014).
20. Becknell, N. *et al*. Atomic structure of Pt_3Ni nanoframe electrocatalysts by *in situ* X-ray absorption spectroscopy. *J. Am. Chem. Soc.* **137,** 15817–15824 (2015).
21. Becknell, N., Zheng, C., Chen, C., Yu, Y. & Yang, P. Synthesis of $PtCo_3$ polyhedral nanoparticles and evolution to Pt_3Co nanoframes. *Surf. Sci.* **648,** 328–332 (2015).
22. Watt, J., Young, N., Haigh, S., Kirkland, A. & Tilley, R. D. Synthesis and structural characterization of branched palladium nanostructures. *Adv. Mater.* **21,** 2288–2293 (2009).
23. Wu, Y. *et al*. Defect-dominated shape recovery of nanocrystals: a new strategy for trimetallic catalysts. *J. Am. Chem. Soc.* **135,** 12220–12223 (2013).
24. Zeng, J. *et al*. Controlling the nucleation and growth of silver on palladium nanocubes by manipulating the reaction kinetics. *Angew. Chem. Int. Ed.* **51,** 2354–2358 (2012).
25. Williams, D. B. & Carter, C. B. *The Transmission Electron Microscope* (Springer, 1996).
26. Ravel, B. & Newville, M. ATHENA, ARTEMIS, HEPHAESTUS: data analysis for X-ray absorption spectroscopy using IFEFFIT. *J. Synchrotron Radiat.* **12,** 537–541 (2005).
27. Zabinsky, S., Rehr, J., Ankudinov, A., Albers, R. & Eller, M. FEFF code for *ab initio* calculations of XAFS. *Phys. Rev. B* **52,** 2995–3009 (1995).
28. Hwang, B.-J. *et al*. Structural models and atomic distribution of bimetallic nanoparticles as investigated by X-ray absorption spectroscopy. *J. Am. Chem. Soc.* **127,** 11140–11145 (2005).
29. Wang, G., Van Hove, M. A., Ross, P. N. & Baskes, M. I. Quantitative prediction of surface segregation in bimetallic Pt–M alloy nanoparticles (M = Ni, Re, Mo). *Prog. Surf. Sci.* **79,** 28–45 (2005).

30. Wang, G., Van Hove, M. A., Ross, P. N. & Baskes, M. Monte Carlo simulations of segregation in Pt–Ni catalyst nanoparticles. *J. Chem. Phys.* **122,** 024706 (2005).
31. Ahmadi, M., Behafarid, F., Cui, C. H., Strasser, P. & Cuenya, B. R. Long-range segregation phenomena in shape-selected bimetallic nanoparticles: chemical state effects. *ACS Nano* **7,** 9195–9204 (2013).
32. Dahmani, C. E., Cadeville, M. C., Sanchez, J. M. & Morán-López, J. L. Ni-Pt phase diagram: experiment and theory. *Phys. Rev. Lett.* **55,** 1208–1211 (1985).
33. Nash, P. & Singleton, M. The Ni-Pt (nickel-platinum) system. *J. Phase Equilib.* **10,** 258–262 (1989).
34. Seo, O. *et al*. Chemical ordering in PtNi nanocrystals. *J. Alloys Compd.* **666,** 232–236 (2016).
35. Vitos, L., Ruban, A., Skriver, H. L. & Kollar, J. The surface energy of metals. *Surf. Sci.* **411,** 186–202 (1998).
36. Cui, C. H. *et al*. Shape-selected bimetallic nanoparticle electrocatalysts: evolution of their atomic-scale structure, chemical composition, and electrochemical reactivity under various chemical environments. *Faraday Discuss.* **162,** 91–112 (2013).
37. Shao, M., Peles, A. & Shoemaker, K. Electrocatalysis on platinum nanoparticles: particle size effect on oxygen reduction reaction activity. *Nano Lett.* **11,** 3714–3719 (2011).
38. Xia, Y., Xia, X. & Peng, H.-C. Shape-controlled synthesis of colloidal metal nanocrystals: thermodynamic versus kinetic products. *J. Am. Chem. Soc.* **137,** 7947–7966 (2015).
39. Zeng, J. *et al*. Controlling the shapes of silver nanocrystals with different capping agents. *J. Am. Chem. Soc.* **132,** 8552–8553 (2010).
40. Niu, Z. & Li, Y. Removal and utilization of capping agents in nanocatalysis. *Chem. Mater.* **26,** 72–83 (2013).

Acknowledgements

The research conducted at Lawrence Berkeley National Laboratory was supported by the US Department of Energy, Office of Science, Office of Basic Energy Sciences, Materials Sciences and Engineering Division, under Contract No. DE-AC02-05CH11231 (surface). Z.N. gratefully acknowledges support from the International Postdoctoral Exchange Fellowship Program 2014. D.K. acknowledges support from Samsung Scholarship. All HRTEM, HAADF-STEM, and EDS mapping made use of the National Center for Electron Microscopy at the Molecular Foundry. XPS data was collected at the Molecular Foundry. We acknowledge M. Marcus and the use of Beamline 10.3.2 at the Advanced Light Source for collection of EXAFS data. The Molecular Foundry and the Advanced Light Source are supported by the Director, Office of Science, Office of Basic Energy Sciences, of the US Department of Energy under Contract No. DE-AC02-05CH11231. We acknowledge P. Alivisatos for access to the Bruker D-8 XRD and E. Kreimer of the Microanalytical Facility in the College of Chemistry, UC Berkeley for access to ICP analysis.

Author contributions

Z.N., N.B. and P.Y. designed the experiments and wrote the paper. Z.N. and N.B. performed the experiments and contributed equally to the work. Y.Y. and N.K. performed HRTEM and HAADF-STEM analysis. D.K. and Z.N. completed XPS analysis. C.C. initiated the work. G.A.S. and P.Y. guided the work. All authors commented on the manuscript.

Additional information

Supplementary information is available in the online version of the paper. Reprints and permissions information is available online at www.nature.com/reprints. Correspondence and requests for materials should be addressed to P.Y.

Competing financial interests

The authors declare no competing financial interests.

Methods

Chemicals. Chloroplatinic acid hexahydrate ($H_2PtCl_6 \cdot 6H_2O$, $\geq$37.5% Pt basis), nickel(II) nitrate hexahydrate ($Ni(NO_3)_2 \cdot 6H_2O$, $\geq$98.5%), oleylamine (technical grade, 70%) and hexane ($\geq$98.5%) were purchased from Sigma-Aldrich. Acetic acid ($\geq$99.7%) was purchased from EMD. Toluene ($\geq$99.9%) was purchased from Fisher Scientific. All chemicals were used as received without further purification.

Synthesis of Pt–Ni rhombic dodecahedra (RD). Aqueous solutions of $H_2PtCl_6 \cdot 6H_2O$ (0.1 g ml^{-1}, 0.4 ml) and $Ni(NO_3)_2 \cdot 6H_2O$ (0.1 g ml^{-1}, 0.35 ml) were mixed with one millilitre of oleylamine in a small vial. The mixture was heated at 120 °C under stirring for one hour, forming a transparent green solution after removal of water. Ten millilitres of oleylamine that had been preheated in a three-necked flask at 160 °C for one hour under nitrogen purging was raised to 230 °C just before the injection. The precursor solution was injected into the three-necked flask immediately after reaching 230 °C. The green reaction solution gradually turned yellow, brown and then black when kept at 230 °C for about one hour. After the growth solution turned black, aliquots were taken out by syringe after 3 min, 10 min and 30 min, and respectively termed as RD-3, RD-10 and RD-30. Before the solution turned black, intermediate products generally termed as pre-RD were collected by stopping the whole batch of reaction to get enough sample for further analysis. All the samples were washed two times by hexane/ethanol mixture, collected by centrifugation (12,000 r.p.m.) after each wash, and then re-dispersed in toluene or hexane.

Chemical corrosion of Pt–Ni rhombic dodecahedra to $Pt_{75}Ni_{25}$ tetradecapod or frame structures. Ten microlitres of oleylamine was added into a toluene dispersion of Pt–Ni rhombic dodecahedra ($\sim$0.5–1 mg ml^{-1}, 2 ml). The colloidal dispersion was briefly sonicated and mixed with two millilitres of acetic acid. The mixture was heated at 90 °C under vigorous stirring for two hours in air to allow chemical corrosion of Pt–Ni rhombic dodecahedra to corresponding $Pt_{75}Ni_{25}$ tetradecapod or frame structures. After corrosion, the products were washed with hexane/ethanol mixture and collected by centrifugation (12,000 r.p.m.). The washed products were re-dispersed in hexane or chloroform.

Characterization. Transmission electron microscopy (TEM) and quantitative energy dispersive spectroscopy (EDS) were performed with a Hitachi H-7650 equipped with EDAX microanalysis. High-resolution TEM (HRTEM) was taken using an FEI Tecnai F20 at an accelerating voltage of 200 kV. High-angle annular dark-field scanning transmission electron microscopy (HAADF-STEM) and EDS mapping were carried out with an FEI TitanX 60-300. X-ray diffraction (XRD) was acquired using a Bruker D-8 General Area Detector Diffraction System (GADDS) with HI-STAR area charge-coupled device (CCD) detector, equipped with a Co-Kα source ($\lambda = 1.789$ Å). Inductively coupled plasma optical emission spectroscopy (ICP-OES) was measured using a PerkinElmer Optima 7000 DV. X-ray photoelectron spectroscopy (XPS) was performed using a PHI 5600 X-ray photoelectron spectrometer. Extended X-ray absorption fine structure (EXAFS) data were collected at the Advanced Light Source Beamline 10.3.2. The data at the Ni K-edge and Pt L_3-edge were calibrated to a Ni foil and Pt foil, respectively. EXAFS data reduction and EXAFS fitting was performed using the IFEFFIT based programs Athena and Artemis[26].

Electrochemical characterization. After chemical corrosion, $Pt_{75}Ni_{25}$ tetradecapods or nanoframes were dispersed in chloroform and added to carbon (Cabot, Vulcan XC-72) in a ratio which produced a loading of 17–20 wt% Pt. The mixture was sonicated in chloroform for 30 to 45 min to complete the loading process. The catalyst was collected by centrifugation (10,000 r.p.m.), washed once with hexanes, and recollected by centrifugation. The resulting catalyst powder was heated at 200 °C in air for 14 h to remove organic surfactants. The $Pt_{75}Ni_{25}$/C catalyst was then dispersed in water with a concentration of 0.5 mg$_{catalyst}$ ml^{-1}. The actual concentration of Pt in the ink was determined by ICP-OES. The catalyst ink was dropcast onto a 5 mm glassy carbon disk (Pine Instruments) in the appropriate volume to achieve 6.9 μg_{Pt} cm^{-2} loading density and allowed to air dry. The commercial Pt/C catalyst (Alfa, $\sim$20 wt% Pt) had a loading density of 7.8 μg_{Pt} cm^{-2}. The electrochemical measurements were conducted in a three-compartment glass electrochemical cell with a Pine rotating disk electrode (RDE) set-up and a Biologic VSP potentiostat. A saturated Ag/AgCl electrode and a Pt wire were used as reference and counter electrodes, respectively, and 0.1 M $HClO_4$ prepared from 67% $HClO_4$ (Sigma-Aldrich) was used as the electrolyte. All potentials are presented versus the reversible hydrogen electrode (RHE). The catalyst was typically held at 0.05 V versus RHE between measurements, and the limits of the cyclic voltammetry (CV) were 0.05–1.02 V. Hydrogen underpotential deposition measurements were performed by saturating the electrolyte with argon gas before collecting the CV at a sweep rate of 50 mV s^{-1}. Electrooxidation of adsorbed CO, or CO-stripping measurements, were performed by purging CO through the electrolyte while holding the potential at 0.05 V. Argon was then purged to remove CO from the electrolyte and the CV was collected at a sweep rate of 50 mV s^{-1}. The ORR measurements were collected under O_2 purging conditions and at 20 mV s^{-1} with an RDE rotation rate of 1,600 r.p.m. The current densities for ORR were corrected for ohmic iR drop.